Int. J. Electrochem. Sci., 15 **(2020)** 9849 – 9863, doi: 10.20964/2020.10.14

International Journal of
ELECTROCHEMICAL
SCIENCE
www.electrochemsci.org

Hierarchically Flower-Like Cobalt Oxide@Doped-Sn Carbon Nanofiber with Core-Shell structure as Anodes for Lithium Ion Battery

Hong Wang[1], Jingyu Zhou[2], Jun Sun[2], Yan Wang[2], Yuejin Ma[1,], Zelin Bai[3,*], Yajun Zhao[2,*], Wenming Zhang[2,*]*

[1] College of Mechanical and Electrical Engineering, Hebei Agricultural University, Baoding 071001, China.
[2] National-Local Joint Engineering Laboratory of New Energy Photoelectric Devices, College of Physics Science and Technology, Hebei University, Baoding, Hebei 071002, China.
[3] Department of Geriatrics, The First Affiliated Hospital to Changchun University of Chinese Medicine, Changchun, Jilin 130021, China.
[*]E-mail: myj@hebau.edu.cn (Y. M), ZelinBai_CCUCM@126.com (Z. Bai), yjzhaohbu@126.com (Y. Zhao), wmzhanghbu@126.com (W. Zhang)

Received: 13 August 2019 / *Accepted:* 19 November 2019 / *Published:* 31 August 2020

Coaxial core-shell hierarchical flower-like cobalt oxide@doped-Sn carbon nanofiber (Co_3O_4@Sn-CNF) prepared by loading Co_3O_4 shells on Sn-CNF that were synthesized via electrostatic spinning and subsequently thermally treated by electrophoretic deposition were used as the anode material for lithium-ion batteries in this paper. The Co_3O_4 shells were not solid but flower-like, provided abundant inner space, facilitated the transfer of lithium ions and electrons and the contact with the electrolyte via the increase in space, increased the electrochemical reaction sites, and improved the electrochemical performance. After the initial discharge specific capacity of 1519 mAh g^{-1}, the discharge specific capacity of the Co_3O_4@Sn-CNF reached 1000 mAh g^{-1} without an obvious capacity decay, and the coulombic efficiency reached 98.6%, indicating the excellent cycle stability of this material. In addition, a specific capacity recovery of 90% demonstrated a remarkable rate performance. The improvement in the electrochemical performance was due to the introduction of the Sn-CNF, which had a good electroconductivity and mitigated the volume deformation due to the elastic deformation of the CNF, in addition to the unique and firm structure.

Keywords: core-shell structure, cobalt oxide, doped-Sn, carbon nanofiber, lithium ion battery.

1. INTRODUCTION

With the advancement of technology, the demand for energy sources continues to grow. Lithium-ion batteries, which are widely used energy storage devices, have been used in mobile phone, laptop,

camera and other portable electronic devices and hybrid cars because of their numerous advantages, such as long cycle life, environmental friendliness, high capacity, high power density, and excellent safety. However, graphite, the most common commercial anode material, has a specific capacity of 372 mAh g^{-1}, which does not meet the current energy demand. Therefore, finding an alternative anode material with improved electrochemical performance has become increasingly important [1-3]. Among these anode materials, cobalt oxide and tin are both very promising candidates to replace graphite and have attracted the attention of many scholars. Co_3O_4, as one of the transition metal oxides (M_xO_y, M = Co, Cu, Fe, or Mn), has been widely used because of its high specific capacity (890 mAh g^{-1}), high safety performance, non-toxicity and low cost [4]. Tin, as a metal, also has a very high specific capacity (959 mAh g^{-1}) [5,6]. However, there are still issues that must be overcome for the application of Co_3O_4 and Sn; namely, rapid capacity decay, poor capacity retention ability and cycle performance must be improved, which are owing to the large volume change that occurs in the material during the lithiation and delithiation processes. Sn, for example, experiences a volume change of approximately 260%, which leads to pulverization of the anode material due to the action of the mechanical stresses. In addition, the loss of electrical contact caused by the volume expansion also results in a reduction in the electrochemical performance of the material [7-11].

At present, there are many studies of Co_3O_4 and Sn that focus on increasing the cycle life, the specific capacity and the reversible capacity in different ways. The primary way to improve the electrochemical performance is to inhibit the huge volume expansion and reduce the loss in the electrical contact by changing the nanostructures of the material or combining it with other elastomeric materials [4]. Different methods, such as electrostatic spinning [12-17], pyrolysis [18], hydrothermal [19-23], and templating methods [24-25], have been applied to the preparation of the anode material to improve its electrochemical performance. However, changing the structure or modifying the surface morphology of the material are the most critical factors in those studies that were used to control the volume expansion, such as nanowire array, nano-cage, Co_3O_4/graphene or carbon nanotube composites, for example, Co_3O_4/carbon core-shell composite nanowires and Sn-Co-C tube-in-tube structures were explored [26-33]. As the structure of the composite material improves, the electrochemical performance improves. An increased electrical conductivity and structural stability result, which can provide additional voids, a large space and a larger specific surface area, enabling an improved electrical contact between the electrode and the electrolyte. All of these factors contribute to the performance of Li-ion batteries. Carbon nanofibers, as a kind of material frequently used for the loading of other materials due to their high electrical conductivity and high surface area, have been used in many areas, including sodium-ion batteries [34], direct methanol fuel cells [35], selective detection of dopamine [36], and biosensors [37] and have been applied in this study.

In this study, we designed a three-dimensional flower-like Co_3O_4@Sn/CNF composite material to improve the rate capability, structure stability, specific capacity, reversible capacity and other electrochemical parameters. Electrospinning, a simple and convenient method to prepare one-dimensional carbon nanofiber [38-41], was used in this study to synthesize the Sn-doped carbon nanofiber. Then, coating the Sn-doped carbon nanofiber with the Co_3O_4 by electrophoretic deposition (EPD) was done, which is a straightforward coating technique that uses an applied electric field [42-49]. Finally, calcination of the composite resulted in the formation of Co_3O_4 three-dimensional structures

from the structures that grew vertically on the surface of the carbon nanofiber during the EPD process; specifically, ternary flower-like Co_3O_4@Sn-CNF composite materials were formed. In this composite, the carbon fiber, which was the core, enhanced the electrical conductivity of the whole material and promoted the transfer of electrons and ions. At the same time, carbon, as an elastic material, had the ability to undergo elastic deformation to decrease the enormous volume change in the Co_3O_4 and Sn during the lithiation and delithiation processes. The three-dimensional network structure also acted as a buffer to mitigate the volume expansion of the Co_3O_4 and Sn and prevent the pulverization of the electrode. Moreover, there was another role for the 3D structure, it provided a large specific surface area and additional void space, which improved the contact between the material and electrolyte during the lithiation and delithiation processes. To a great extent, Co_3O_4 and Sn improved the specific capacity of the composite, and along with the carbon, they contributed to maintaining the structural stability, which is one of the keys to improving the electrochemical performance.

2. EXPERIMENTAL

2.1 Preparation of the carbon nanofiber

The polymer solution was prepared by dissolving the polyacrylonitrile (PAN, M_w = 150,000, Aldrich) in N, N-dimethylformamide (DMF, Aladdin) (mass ratio, PAN: DMF = 9:1), which was then stirred gently at room temperature until the polymer solution became homogeneous and transparent. The electrospinning process was conducted in an electrospinning machine equipped with a variable high-voltage power supply. The polymer solution was placed in five 10 mL syringes with a capillary tip connected with the anode of the high-voltage power supply. The metal roller, as a collector, was wrapped with aluminium foil, and the area where the carbon nanofiber collected were connected to the cathode of the power supply. In this experiment, the applied voltage was 27 kV, the distance between the tip and the collector was 15 cm, and the flow rate of the solution was 15 μL min^{-1}. The collected fibers were heated to 270 ^{0}C in air at a rate of 1 ^{0}C min^{-1} to stabilize the fibers and maintained at this temperature for 1 h. Then, the stabilized fibers were carbonized by continuing the heating process to 1000 ^{0}C in a nitrogen atmosphere at a rate of 5 ^{0}C min^{-1} and maintained for 1 h. Finally, the CNF were prepared after cooling to room temperature.

2.2 Preparation of the Sn-doped carbon nanofiber

The preparation of Sn-doped carbon nanofiber was similar to that of carbon nanofiber. There were two main differences: first, during the preparation of the polymer solution, the $Sn(CH_3COO)_2$ (Aldrich) was added to the PAN and DMF solution after being stirred to form a homogeneous solution (mass ratio, DMF: PAN: $Sn(CH_3COO)_2$ = 23:2:1). Second, during the heat treatment, stabilization was carried out at 230 ^{0}C for 1 h at a rate of 1 ^{0}C min^{-1}, and carbonization was carried out at 800 ^{0}C for 1 h.

2.3 Preparation of the Co_3O_4 powder

The preparation of the Co_3O_4 powder was as follows: 0.5 g $Co(NO_3)_2 \cdot 6H_2O$ (Macklin) was calcined at 250 ^{0}C at a rate of 5 ^{0}C min^{-1} in air for 1 h and then cooled to room temperature. The reaction mechanism as shown here [50]:

$$3Co(NO_3)_2 \rightarrow Co_3O_4 \downarrow +6NO_2 \uparrow +O_2 \uparrow \quad (1)$$

2.4 Preparation of the Co_3O_4/carbon nanofiber

The apparatus described in a previous work was used for the EPD process herein [4,51]. The CNF, were used as the cathode, and the Pt wires were used as the anode and spaced 3 cm apart. This system was immersed in the $Co(NO_3)_2 \cdot 6H_2O$ ethanol solution, which contained the defined amount of deionized water to make the dispersed $Co(NO_3)_2$ more homogeneous. The applied voltage was 10 V, and it was sustained for 2 h. Then, the CNF was removed and washed with ethanol numerous times. After drying at room temperature, the CNF was heated at 250 ℃ in air and finally formed the three-dimensional flower-like Co_3O_4@CNF structures.

2.5 Preparation of the Co_3O_4@Sn-CNF

This work was the same as that described in Section 2.4, except that Sn-doped CNF were used instead of undoped CNF.

2.6 Characterizations techniques

The morphologies of all samples were studied by using field-emission scanning electron microscopy (FE-SEM). The size, distribution, and coating of the particles were observed by using transmission electron microscopy (TEM). The degree of the crystallinity in the samples was studied by using X-ray diffraction (XRD). The electrochemical studies were conducted by using a coin cell (type CR2032) that was assembled in a glove box filled with argon. The copper foil was coated by a slurry consisting of 80% active material, 10% super P (as the conductive agent), and 10% hydroxymethyl cellulose (CMC, as the binder), this material was added to a proper amount of deionized water and used as the working electrode. The Li foil was used as the counter electrode and reference electrode, and there was a polypropylene film (Celgard® 2400) between the copper foil and Li foil. The electrolyte used in this work was a solution of 1 M $LiPF_6$ dissolved in a mixed solution of ethylenecarbonate (EC)/dimethyl carbonate (DMC) (1:1, V:V) (Zhangjiagang Guotai Huarong Chemical New Material Co.). All other components, such as the battery case, slurry, and polypropylene film, were dried at 100 ^{0}C in a vacuum to remove the oxygen and the water, and the amount of the oxygen and water in the glove box was less than 0.1 ppm. Electrochemical impedance spectroscopy (EIS), used to measure the electrical conductivity, and obtain the cyclic voltammetry (CV), to determine the electrochemical reaction, these measurements were all conducted on an electrochemical workstation (CHI660E, CH Instruments,

Shanghai, China). The discharge-charge tests, including cycle performance and the rate performance tests, were conducted in a battery cycling system (CT2001A, LAND Electronics, Wuhan, China).

3. RESULTS AND DISCUSSION

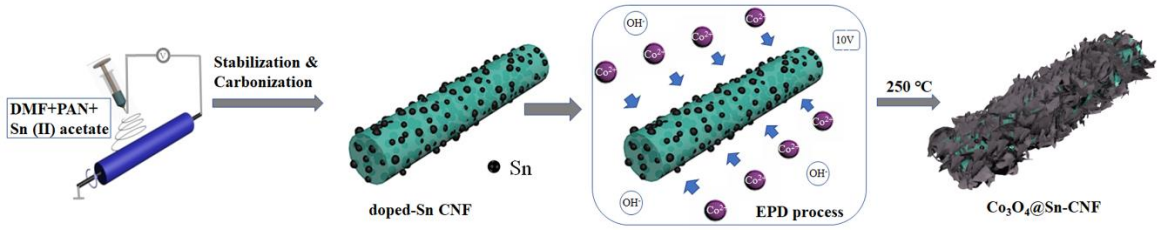

Figure 1. Schematic illustration of the preparation process of Co_3O_4@Sn-CNF.

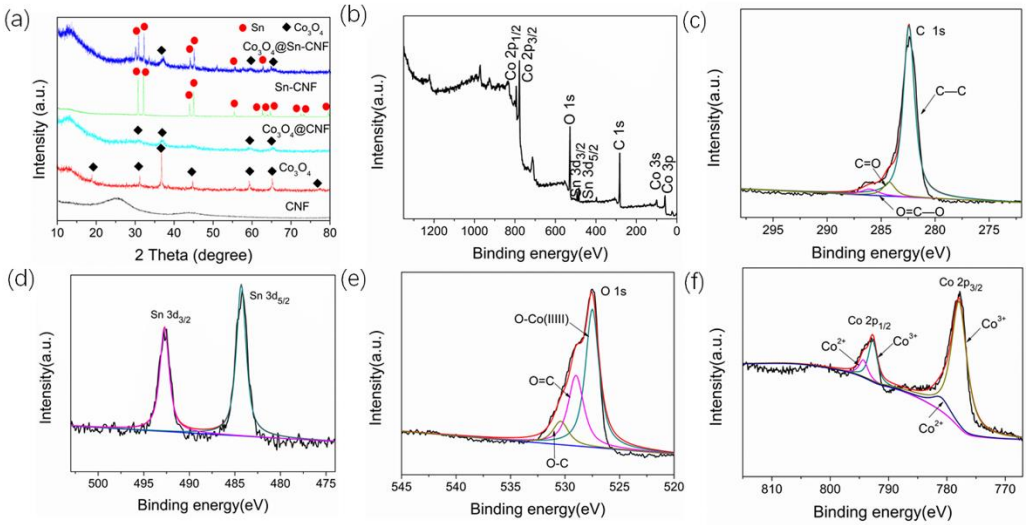

Figure 2. (a) XRD patterns of CNF, Sn-CNF, Co_3O_4, Co_3O_4@CNF, and Co_3O4@Sn-CNF; (b) XPS images of Co_3O_4@Sn-CNF composite nanofiber; (c) XPS images of C 1s; (d) XPS images of Sn 3d; (e) XPS images of O 1s; (f) XPS images of Co 2p.

Electrophoretic deposition (EPD), a straightforward physical process, was applied to coat the Co_3O_4 onto the CNF or Sn-CNF, which had the same mechanism. Considering coating the Co_3O_4 on the CNF. In this study, the CNF and Pt wires were used as the cathode and anode, and both were immersed in the $Co(NO_3)_2 \cdot 6H_2O$ ethanol solution. Co^{2+} in the cobalt nitrate shifted to the cathode and adsorbed on the surfaces of the CNF, which became positively charged as CNF-Co^{2+} when the electric field was applied. Moreover, NO_3^- in the cobalt nitrate was electrochemically reduced with the H_2O and produced OH^-, which then moved towards the cathode and reacted with the Co^{2+} to form $Co(OH)_2$ on the surfaces of the CNF. Finally, Co_3O_4-CNF were obtained by heating the CNF-$Co(OH)_2$ to 250 ^{0}C for 2 h. The reaction mechanism of this process is shown below [51-53]:

$$CNF + Co^{2+} \xrightarrow{adsorption} CNF - Co^{2+} \quad (2)$$

$$NO_3^- + H_2O + 2e^- = NO_2^- + 2OH^- \quad (3)$$

$$2H_2O + 2e^- = 2OH^- + H_2 \quad (4)$$

$$CNF - Co^{2+} + 2OH^- = CNF - Co(OH)_2 \quad (5)$$

$$CNF - 3Co(OH)_2 \overset{250℃}{=} CNF - Co_3O_4 + 2H_2O + H_2 \quad (6)$$

As shown in Fig. 2(a), the crystalline texture of the CNF, Sn-CNF, Co_3O_4, Co_3O_4@CNF, and Co_3O_4@Sn-CNF was analysed by using X-ray diffraction (XRD). The XRD pattern of the CNF revealed two broad and smooth peaks at approximately 2θ = 25° and 44°, the first peak proved the formation of a typical amorphous structure [4, 51], and the second peak as weak, indicating the existence of some ordered carbon in the carbon fibers [54]. The crystalline structure of Co_3O_4 powder was indicated by the peaks at 2θ = 19.0°, 31.3°, 36.8°, 44.8°, 59.4°, 65.2°, and 77.3°, which corresponded to the (111), (220), (311), (400), (511), (440), and (533) planes. These results indicate a space group of spinel Co_3O_4 (JCPDS No. 43-1003), and the high peak intensities indicate the existence of bulky particles in the powder. The Co_3O_4 peaks in the Co_3O_4@CNF and Co_3O_4@Sn-CNF were almost the same as the peaks in the Co_3O_4 powder, demonstrating that cobalt nitrate completely converted to Co_3O_4 during the EPD process and subsequently during the calcination process. In addition, compared to that of the Co_3O_4 powder, the Co_3O_4 peaks in the Co_3O_4@CNF and Co_3O_4@Sn-CNF were weaker in intensity, indicating that the Co_3O_4 that formed on the surface of the fibers had a nano-scale structure, the peaks were also wider in width because of the slow loading of the $Co(OH)_2$ on the surface of the fibers due to the small voltage (10 V) during the EPD process. The crystallization of Sn was indicated by the peaks at 2θ = 30.6°, 32.0°, 43.9°, 44.9°, 55.3°, 62.5°, 63.8°, 64.6°, 72.4°, 73.1°, and 79.5° that could be indexed to the (200), (101), (220), (211), (301), (112), (400), (321), (420), (411), and (312) peaks. The peaks were consistent with the tetragonal structure of metallic Sn with a space group of $I4_1/amd$ (JCPDS No. 65-0296). The Co_3O_4@Sn-CNF had similar peaks to those for the Sn-CNF, indicating that the microstructure of the Sn was not influenced during the EPD and subsequently calcination processes. The decrease in the peak intensities indicated that the coating of the flower-like Co_3O_4 shell on the Sn-CNF was intact.

Fig. 2(b-f) shows the XPS images of the hierarchical flower-like Co_3O_4@Sn-CNF composite nanofiber, and Fig. 2 (b) shows the XPS images of the whole composite material, from which we can observe the existence of Co, C, O and Sn. Fig. 2(c) shows the intercepted image of the C element in the 1s orbit, from which we can see the three peaks at binding energies of 286.0 eV, 284.2 eV and 282.4 eV that correspond to three functional groups of O=C-O, C=O and C-C, respectively. Fig. 2 (d) shows the XPS images of the Sn element in the 3d orbit, and the peaks at 483.7 eV and 492.7 eV correspond to the two atomic states of Sn 3d5/2 and Sn 3d3/2 respectively. Combined with Fig. 2 (b), it can be determined that the content of the Sn element in the material was low. The images of the O element in 1s orbit in Fig. 2 (e) contained two weak peaks, indicating the presence of the two chemical bonds of C=O and C-O at 529.0 eV and 530.4 eV, respectively, where the O element was not the one in the Co_3O_4, rather, the O element may have been left from the preparation and calcining processes, similar to that of the C element in 1s orbit, while the main peak near 527.5 eV corresponds to the O element in spinel cobalt oxide. Fig. 2(f) shows the XPS image of the Co element containing two peaks of Co 2p1/2 and Co 2p3/2. With a high binding energy, the peak at Co 2p1/2 consists of two peaks with binding energies of 794 eV and 792 eV, which corresponds to the combined state of Co^{2+} and Co^{3+}, respectively. Similarly, the peak at Co 2p3/2 also consisted of two chemical bonds peaks corresponding to Co^{2+} and Co^{3+}, located at 781.1 eV and 778.0 eV, respectively.

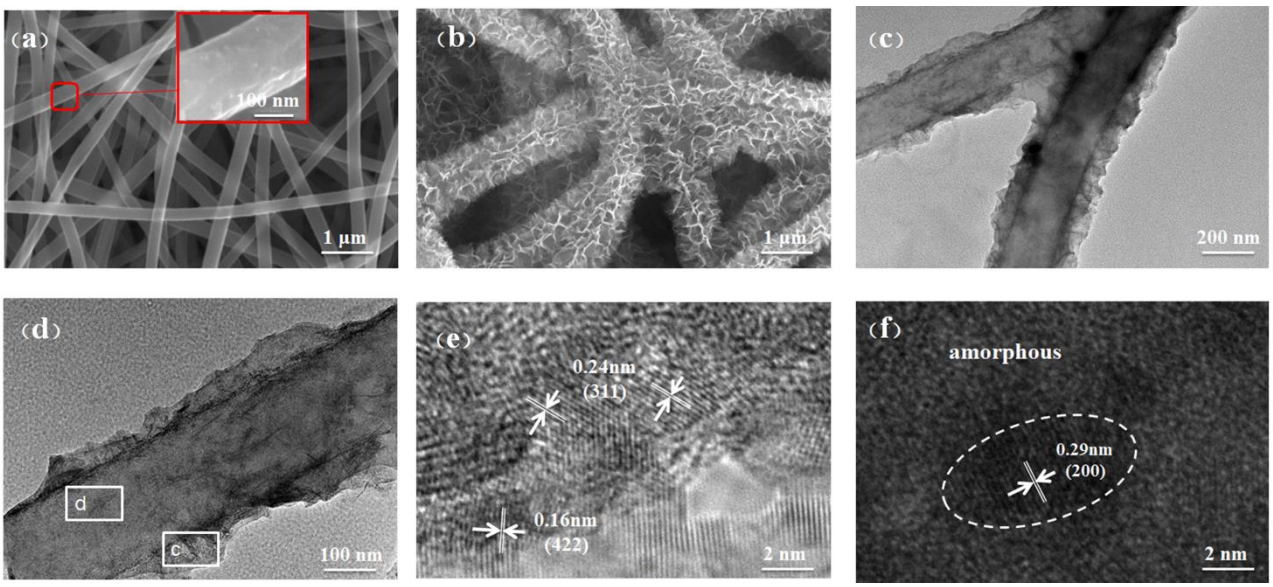

Figure 3. (a-b) SEM images of Sn-CNF and Co_3O_4@Sn-CNF; (c-d) TEM images of Co_3O_4@Sn-CNF; (e-f) high-resolution TEM image of Co_3O_4@Sn-CNF.

Fig. 3(a-b) shows the SEM images for the surface of the Sn-CNF and Co_3O_4@Sn-CNF. The Sn-CNF shown in Fig. 3(a) had a smooth surface and uniform diameter, of approximately 300 nm, indicating that tin existed in the interior of the fibers and mixed with the carbon, as a result of the mixing of the stannous acetate and carbon precursor during the spinning process. In addition, Sn-CNF major axis was aligned along the winding direction of the metal roller and had an interconnected morphology, which increased the conductivity. The Co_3O_4@Sn-CNF shown in Fig. 3(b) had a three-dimensional (3D) hierarchical flower-like morphology, and the Co_3O_4 shell (from the Co_3O_4 that grew vertically on the surface of the CNF during the EPD process) was coated on the CNF core. The growth of the flower-like structure, mainly due to the $Co(OH)_2$ that adsorbed on the π-electrons between the carbons, and the existence of the tin reduced the amount of carbon, leading to a decrease in the π-electrons, which is the reason why the density of the Co_3O_4@Sn-CNF nanosheets decreased. The Sn-CNF covered by the Co_3O_4 during the EPD process increased the diameter from 300 nm to 1 μm, but the incremental volume was mesoporous, and had a substantial amount of space, which improved the contact between the material and the electrolyte, consequently increasing the transfer of the Li-ions and electrons. In addition, the interconnected Sn-CNF, increased the conductivity, and the 3D ternary hierarchical flower-like morphology, enhanced the stability, both of which improved the mechanical and electrochemical properties.

Fig. 3(c-f) shows the TEM image and a high resolution image of the Co_3O_4@Sn-CNF. Fig. 3(c) and (d) show a layer of the coaxial three-dimensional morphology of the Co_3O_4 shell coated on the fiber, which had a uniform size and a diameter of 200 nm. It can be clearly seen when observing the surface that there was a dark stripe in fig. 3(d), which was actually Co_3O_4 flakes that grew on the fiber surface, which confirmed the morphology observed during SEM. Two areas were used to conduct the high-resolution TEM analysis, and the results are shown in Fig. 3(e) and (f). The area in Fig. 3(e) comprised the shell of the materials, and lattice fringes were observed, which indicated the high degree of

crystallinity in the Co_3O_4, which improved the electrochemical performance. The lattice spacing in Fig. 3(e) is 0.24 and 0.16 nm, corresponding to the (311) and (422) Co_3O_4 lattice planes, respectively, indicating the existence of Co_3O_4 with a spinel structure. The intercepted area in Fig. 3(f) had less Co_3O_4. It was observed that most of the particles were amorphous, proving the production of amorphous carbon. The dotted line area had a satisfactory crystal lattice, corresponding to the Sn nanoparticles inserted in the fiber. The 0.29 nm lattice spacing corresponds to the (200) crystal face of the quartet crystal Sn. This result indicated that the Co_3O_4 shell comprised flake-like Co_3O_4, which provided abundant space and increased the contact with the electrolyte.

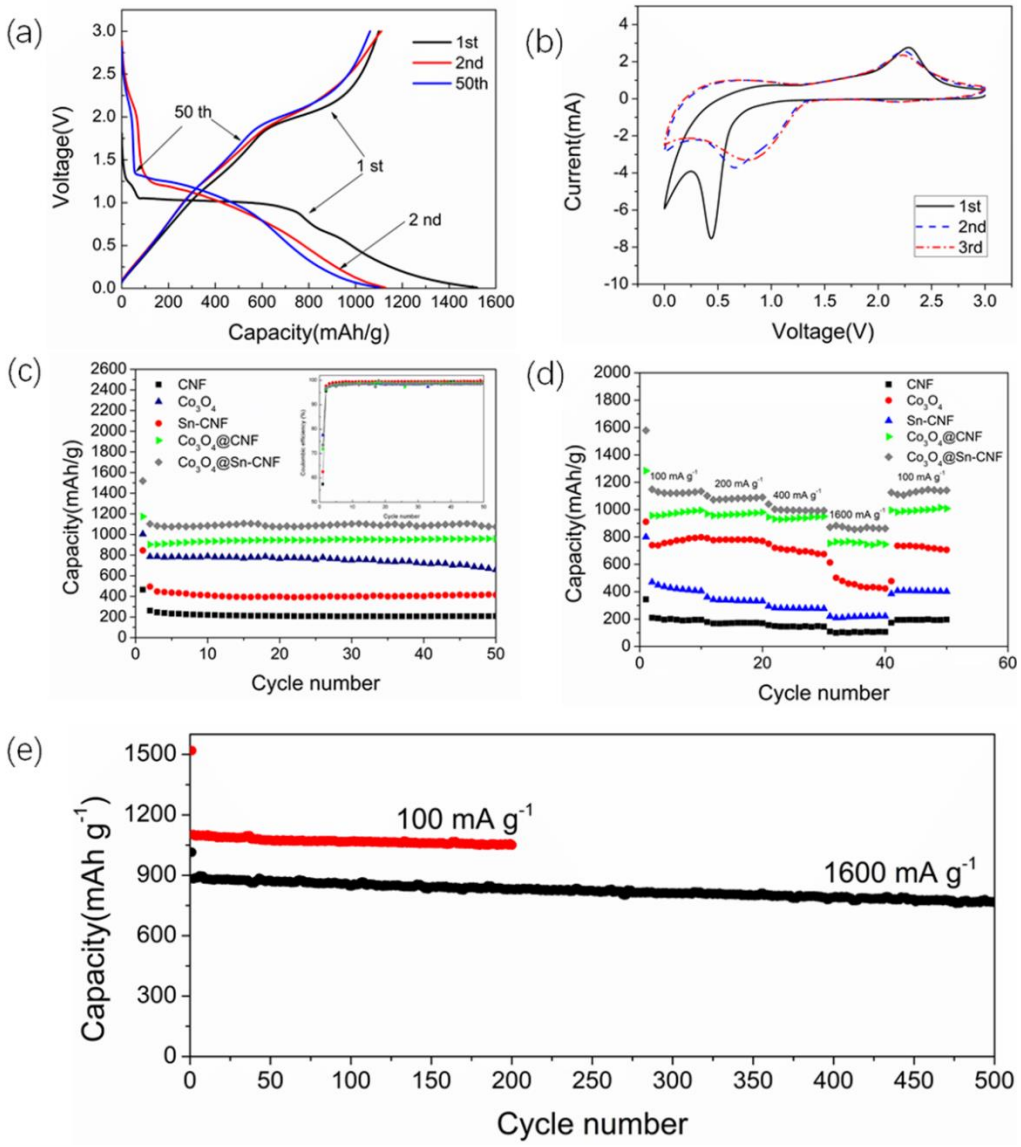

Figure 4. (a)Voltage profile of Co_3O_4@Sn-CNF at 100 mA g^{-1} in 1M $LiPF_6$/EC/DMC; (b) Cyclic voltammograms of Co_3O_4@Sn-CNF at 0.2 mV s^{-1} scan rate in 1M $LiPF_6$/EC/DMC; (c) Cycle performance and coulombic efficiency of CNF, Sn-CNF, Co_3O_4, Co_3O_4@CNF, and Co_3O_4@Sn-CNF at 100 mA g^{-1} in 1M $LiPF_6$/EC/DMC; (d) Rate Performance of CNF, Sn-CNF, Co_3O_4, Co_3O_4@CNF, and Co_3O_4@Sn-CNF at different current densities; (e) long-term cycle of Co_3O_4@Sn-CNF under the current densities of 100 and 1600 mA g^{-1}.

Table 1. Comparison of the electrochemical lithium-storage performance of the Co_3O_4@Sn-CNF presented in this work and previously reported Co_3O_4-based anode materials.

Materials	Morphology	Reversible capacity (mA h g^{-1})	Current density (mA g^{-1})	Ref. No
NGr-Co_3O_4	Nanolayers	780 mA h g^{-1}/50th	1000 mA g^{-1}	57
Co@Co_3O_4/CNT	Nanocomposites	760 mA h g^{-1} /350th	1000 mA g^{-1}	58
Co_3O_4	Nanorods	628 mA h g^{-1}/350th	1000 mA g^{-1}	21
Co_3O_4/carbon	Nanosheets	940 mA h g^{-1}/600th	1000 mA g^{-1}	56
Co_3O_4/CNF	Nanofibers	400 mA h g^{-1}/700th	0.5 C (1C=890 mA g^{-1})	13
Co_3O_4@TiO_2	Nanofibers	525 mA h g^{-1}/100th	500 mA g^{-1}	63
Co_3O_4	Nanoneedles	842.9 mA h g^{-1}/300th	500 mA g^{-1}	23
T-Co_3O_4/Co@NC	Nanotubes	689.2 mA h g^{-1}/400th	500 mA g^{-1}	61
Co_3O_4	Nanoparticles	585.6 mA h g^{-1}/200th	50 mA g^{-1}	65
Co_3O_4@NC	Nanotparticles	1017 mA h g^{-1}/100th	100 mA g^{-1}	55
N,P-codoped C/Co_3O_4	Sponge-like composite	927 mA h g^{-1}/100th	100 mA g^{-1}	62
Co/Co_3O_4	Metal–organic frameworks	903 mA h g^{-1}/100th	100 mA g^{-1}	60
Co_3O_4/graphene	Nanotubes	961.4 mA h g^{-1}/80th	100 mA g^{-1}	64
Co_3O_4/GF	Metal-organic framework	986 mA h g^{-1}/250th	100 mA g^{-1}	59
Co_3O_4@Sn-CNF	Nanofibers	1050 mA h g^{-1}/200th	100 mA g^{-1}	This work

Fig. 4(a) represents the initial, second and fiftieth discharge and charge profile of Co_3O_4@Sn-CNF composite electrodes in the voltage range from 0-3 V at 100 mA g^{-1}. The initial discharge capacity for the Co_3O_4@Sn-CNF was 1519 mAh g^{-1}, and the initial charge capacity was 1033 mAh g^{-1}, showing a low initial coulombic efficiency of 72%, this was likely due to the irreversible loss of lithium, namely the formation of a solid electrolyte interface (SEI) film on the surface of the material during the discharge process. Then, the coulombic efficiency of the Co_3O_4@Sn-CNF steeply increased to 98.4% during the second discharge and charge processes, having a 1126 mAh g^{-1} discharge e capacity and 1109 mAh g^{-1} charge capacity and stabilizing at approximately 98%.

The first three cyclic voltammograms from the button cell fabricated by the Co_3O_4@Sn-CNF composite at a 0.2 mV s^{-1} scan rate in the range of 0.02-3 V are shown in Fig. 4(b). In the first scan, the cathodic peak at 0.48 V corresponds to the formation of amorphous Li_2O, Li_xSn and a partially

irreversible solid electrolyte interface film (SEI film) on the surface of the material. The potential plateaus observed at 0.6 V were derived from the appearance of Sn during the Li^+ deintercalation process. The anodic peak at 2.3 V was involved in the reversible redox reaction, including the conversion from Co_3O_4 to Co/Li_2O and Sn to Li_xSn, as described in Eqs. (7) and (8), respectively, and the anodic peak corresponds to the oxidation of Co and Li_xSn. In the second scan, the cathodic peak observably decreased, proving the formation of a SEI film. In the latter scan, the cathodic peak continued to decrease, and the potential of the current peaks increased due to the facile polarization due to the good reversibility. Moreover, the shift of the cathodic peak to an increased potential as the scan continued depended on the unique structure and high specific surface area of the flower-like Co_3O_4 shells. After the first scan, the good overlap of the pattern certified the good reversibility of the composite.

$$Co_3O_4 + 8Li^+ + 8e^- \Leftrightarrow 4Li_2O + 3Co \quad (7)$$

$$\mathrm{Sn} + xLi^+ + xe^- \Leftrightarrow Li_xSn (0 < x < 4.4) \quad (8)$$

The cycle performance and coulombic efficiency of the CNF, Sn-CNF, Co_3O_4, Co_3O_4@CNF structures, and Co_3O_4@Sn-CNF structures at a current density of 100 mA g^{-1} in the voltage range from 0 to 3 V are shown in Fig. 4(c). The initial discharge specific capacity was 464 mAh g^{-1} and then decreased and stabilized at 208 mAh g^{-1}, giving a steady coulombic efficiency of 99.4% and indicating that the CNF had an excellent capacity retention and cycle performance despite their low capacity. Compared to that for the pure CNF, the doped-Sn CNF had a higher specific capacity with an initial discharge specific capacity of 845 mAh g^{-1}. This value was maintained at approximately 400 mAh g^{-1}, which indicated a coulombic efficiency of 99.5% and that the doped-Sn effectively improved the electrochemical performance and specific capacity of the fibers. Furthermore, the good cycling stability and remarkable specific capacity and coulombic efficiency indicate that the CNF hindered the volume change of the Sn commendably during the intercalation and deintercalation processes. After reaching the capacity of 1003 mAh g^{-1} in the first discharge process, the charge and discharge specific capacity of the Co_3O_4 powder decayed constantly until it reached 657 mAh g^{-1} for the fiftieth discharge due to the major volume change during the cycle process. Compared to that of the initial discharge capacity of the Co_3O_4@CNF composites (1174 mAh g^{-1}), the Co_3O_4@Sn-CNF had an amazing initial discharge capacity of 1519 mAh g^{-1}, and stabilized at approximately 1000 mAh g^{-1} without a substantial decrease in the capacity, and the coulombic efficiency stabilized at approximately 98.5% simultaneously. These results suggest that the Co_3O_4@Sn-CNF had an excellent discharge capacity and cycling stability. The electrochemical performance was closely related to the rate capability and electrochemical stability. The electrochemical stability of the Co_3O_4@Sn-CNF was substantially improved because of two factors: the introduction of the Sn-CNF with excellent electrical conductivity and the existence of the hierarchical flower-like Co_3O_4 shells. Introducing the Sn-CNF effectively improved the electrochemical performance of the composites not only because of the high electrical conductivity, but also because of the one-dimensional structure of the Sn-CNF. Compared to that of other carbon particles, the one-dimensional fibers provided a 1D electron path that decreased the resistance during the electron transfer and therefore expedited the lithiation and delithiation processes. The existence of the hierarchical flower-like Co_3O_4 shells that grew vertically from the fiber core also improved the electrochemical performance. This flower-like structure was not solid but had abundant inner space, signifying an increase in the specific surface area, better contact with the electrolyte and additional electrochemical reaction sites on

the Co_3O_4 shell. In addition, the Co_3O_4 shell and doped-Sn inevitably experienced deformation during the lithiation process. With the lithium was inserted into the composites, the Co_3O_4 shell started to expand along the radial direction and the Sn-CNF were compressed. At this moment, the CNF played a critical role in reducing the mechanical stress from the Co_3O_4 and Sn because of the good elastic properties of the CNF. Hindering the volume expansion of the Co_3O_4 and Sn effectively hinders the capacity fading. Moreover, the remarkable structural stability of the Co_3O_4@Sn-CNF structures also contributed to the improvement in the rate performance and cycle performance.

Fig. 4(d) illustrates the corresponding discharge specific capacity of the CNF, Sn-CNF, Co_3O_4, Co_3O_4@CNF structures, and Co_3O_4@Sn-CNF structures at different current densities. The data includes fifty discharge and charge cycles and a change in the current density every ten cycles in the following order: 100, 200, 400, 1600, and 100 mA g^{-1}. In the first forty cycles, the specific capacity of the composites constantly decreased with increasing current density because of the polarization phenomenon during the electrochemical reaction process after increasing the current density. At the beginning of the forty-first cycle, the applied current density was changed to 100 mA g^{-1} to study the percent recovery in the specific capacity by comparing the discharge specific capacity of the first ten cycles. Compared to the steady discharge capacity at various current densities and the excellent recovery of the specific capacity, the Co_3O_4 powder capacity decayed quickly at high current densities (1600 mA g^{-1}), from 613 to 423 mAh g^{-1}, and after the current density was changed to 100 mA g^{-1}, the percent recovery of specific capacity was only 60%. The discharge specific capacities of Co_3O_4@Sn-CNF at 100, 200, 400, 1600, and 100 mA g^{-1} were 1120, 1080, 1000, 850, and 1100 mAh g^{-1}, respectively, and the discharge specific capacities were very stable. The percent recovery of the specific capacities was greater than 90% during the last ten cycles, indicating a remarkable electrochemical stability, which was closely related to the rate performance and electrochemical performance. The reason for the improvement in the rate performance is similar to that for the cycle performance; namely, the reduction effect and electrical conductivity of the CNF, the unique structure of the Co_3O_4 shells and the stability of the whole structure.

Fig. 4(e) shows the long-term cycle results for the Co_3O_4@Sn-CNF composite at current densities of 100 and 1600 mA g^{-1}. As shown in the figure, at a current density of 100 mA g^{-1}, the composite material maintained excellent cyclic stability and still had a capacity of 1050 mAh g^{-1} after 200 cycles, with a capacity retention rate of 94%, which was mainly due to the introduction of the Sn-CNF and their ability to improve the structural stability of the material. The electrochemical lithium-storage performance of the electrodes developed in this study was compared to that of similar Co_3O_4-based electrodes, as shown in Table 1, where the morphologies are also included. Clearly, the Co_3O_4@Sn-CNF electrode presented a higher reversible capacitance at a given current density of 100 mA g^{-1} among all similar electrode materials reported in the literature [13,21,23,55-65], suggesting that the electrode material can be a good candidate as a high-performance anode material. However, at a current density of 1600 mA g^{-1}, the composite capacity remained at 760 mAh g^{-1}, and the capacity retention rate was 86% after 500 charge and discharge cycles. This was mainly due to the damage to the surface morphology of the material from additional ions and electrons intercalating and deintercalating at high current densities and the offset of the electrode potential from the balanced potential due to the simultaneous appearance of a large current, which resulted in a decrease in the capacity retention rate.

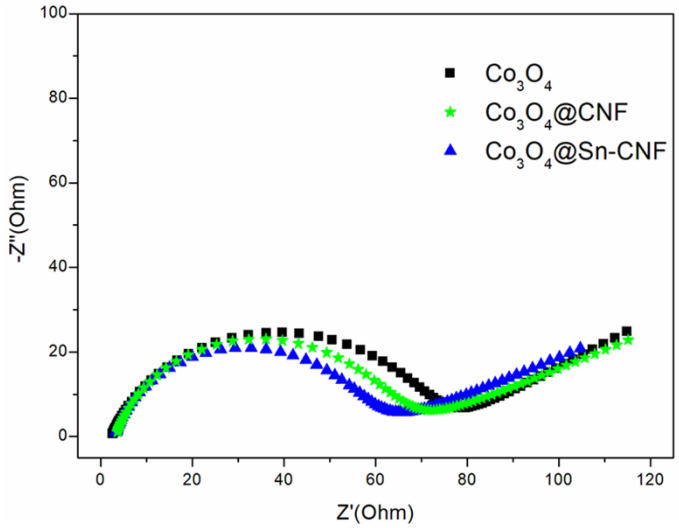

Figure 5. AC impedance spectra of Co_3O_4, Co_3O_4@CNF and Co_3O_4@Sn-CNF in 1M $LiPF_6$/EC/DMC (EC: DMC= 1).

Fig. 5 shows the electrochemical impedance spectroscopy (EIS) curves for the Co_3O_4, Co_3O_4@CNF structures and Co_3O_4@Sn-CNF structures using Nyquist plots in the range of 0.01 Hz to 100 kHz. The changes in the EIS curves for the different materials provided information on the charging and discharging process and the electronic and ionic conductivities of the active materials. Generally, the EIS curves for Li-ion batteries are similar and mainly includ two parts: a semicircle in the high-frequency regime and a linear portion in the low-frequency regime. The information obtained from the EIS curves had two noteworthy points: the intrinsic electrical resistance (R_Ω) and the charge-transfer resistances (R_{ct}). The intersection of the semicircle in the high-frequency regime and the real axis represents the internal resistance relating to the intrinsic electrical resistance (R_Ω) of the active material, the resistance between electrolyte and electrodes, and the contact resistance at the interface between the electrodes and current collector. However, at the same experimental conditions, the latter two factors do not play an important role in this study. Hence, the internal resistance was primarily related to the intrinsic electrical resistance (R_Ω) of the active material, which is why the internal resistance of Co_3O_4 powder was almost the same as that of the Co_3O_4@Sn-CNF and Co_3O_4@CNF structures (all 3 Ω). The size of the semicircle in the high-frequency regime was decided by the charge-transfer resistance (R_{ct}), and a very intuitive reflection of this value is the diameter of the semicircle. The charge-transfer resistance (R_{ct}), which is generated at the two-phase interface between the electrode and the electrolyte, represents the electron transfer ability and the difficulty of the electrochemical reaction at this interface, and the major factors that influence this process are the conductivity of the active material and the surface morphology, which primarily includes the specific surface area and the size and amount of the pore of the material. In another way, the lower the value the charge-transfer resistance (R_{ct}) is, the faster the transfer of the charge, and the more active it is during the electrochemical reaction. In this paper, the charge transfer resistance of the Co_3O_4, Co_3O_4@CNF structures and Co_3O_4@Sn-CNF structures was 70 Ω, 60.5 Ω and 55 Ω, respectively. The R_{ct} of the Co_3O_4@Sn-CNF structures was smaller than that of the Co_3O_4@CNF structures because compared to that of the pure carbon fiber, the Sn-doped carbon fiber

contained abundant tin, which has a better conductivity. The Co_3O_4@CNF and Co_3O_4@Sn-CNF structures are still is excellent anode electrode materials in view of the outstanding discharge specific capacity. In comparison to that of the pure Co_3O_4 powder, the R_{ct} of Co_3O_4@Sn-CNF was much smaller, which was due to (a) the use of the Sn-CNF to enhance the conductivity; (b) the excellent morphology of the material surface, including the high specific surface area and the abundant inner space, to facilitate the transfer of charge and the permeation of electrolyte; and (c) the structural stability of the hierarchical flower-like Co_3O_4 shell. These three factors cooperatively facilitated the charge transfer and permeation of the electrolyte, decreased the resistance, reduced the ion inset distance in the nanometre range and improved the electrochemical performance.

4. CONCLUSIONS

A novel three-dimensional (3D) coaxial core-shell hierarchical flower-like Co_3O_4@doped-Sn CNF was prepared by loading Co_3O_4 shells onto the Sn-CNF synthesized via electrostatic spinning and subsequently thermally treated by electrophoretic deposition; this structure was used as the anode material for lithium-ion batteries in this paper. The hierarchical flower-like Co_3O_4 shell played an important role in the improvement of the cycle stability and rate performance by providing high specific capacity. After the initial discharge capacity of 1519 mAh g^{-1}, the discharge capacity stabilized at 1000 mAh g^{-1} without an evident capacity decay after fifty discharge and charge cycles, which is superior to the discharge capacity of pure Co_3O_4 powder (657 mAh g^{-1}), Co_3O_4@CNF composites (890 mAh g^{-1}), and pure CNF (200 mAh g^{-1}). In the rate performance tests, the Co_3O_4@Sn-CNF composites revealed excellent recovery of the specific capacity (90%), which is superior to that of Co_3O_4 powder (60%). The wonderful rate performance and cycle stability were due to two factors: the Co_3O_4 shell and doped-Sn CNF. The abundant inner space generated from the flower-like Co_3O_4 shell increased the electrochemical reaction sites and the contact with the electrolyte and promoted the transfer of the lithium-ions, leading to an increased velocity for the lithiation process and an improvement in the electrochemical performance. In addition, the Sn-CNF had a good electrical conductivity, and compared to that of other types of carbon, the Sn-CNF had a one-dimensional structure, which provided 1D pathways for the electrons, reduced the resistance of the electrons, and tremendously facilitated the electron transfer during the lithiation and delithiation processes. The CNF had commendable elastic properties and restrained the volume expansion, efficiently enhancing the rate performance and cycle capacity of the Co_3O_4@Sn-CNF composite materials.

ACKNOWLEDGMENTS
We gratefully acknowledge the financial support from the following sources: National Natural Science Foundation of China (NSFC) (Grants 51607054), Young Talent of Hebei Province (NO.70280011808, 70280016160250), Hebei Province Outstanding Youth Fund (A2018201019, A2017201082), Undergraduate innovation and entrepreneurship training program (2019153).

References

1. V. Etacheri, R. Marom, R. Elazari, G. Salitra and D. Aurbach, *Energ. Environ. SCI.*, 4 (2011) 3243.
2. K. Kang, Y. S. Meng, J. Breger, C. P. Grey and G. Ceder, *Science*, 311 (2006) 977.

3. N. -S. Choi, Z. H. Chen, S. A. Freunberger, X. L. Ji, Y. -K. Sun, K. Amine, G. Yushin, L. F. Nazar, J. Cho and P. G. Bruce, *Angew. Chem., Int. Ed.,* 51 (2012) 9994.
4. S. -H. Park and W. -J. Lee, *J. Power Sources*, 281 (2015) 301.
5. L. Sun, H. C. Si, Y. X. Zhang, Y. Shi, K. Wang, J. G. Liu and Y. H. Zhang, *J. Power Sources*, 415 (2019) 126.
6. A.P. Nowak, J. Solid State Electrochem., 22 (2018) 2297.
7. K. Hirai, T. Ichitsubo, T. Uda, A. Miyazaki, S. Yagi and E. Matsubara, *Acta Mater.,* 56 (2008) 1539.
8. Y. Tian, A. Timmons and J. R. Dahn, *J. Electrochem. Soc*., 156 (2009) A187.
9. S. B. Yang, X. L. Feng, S. Ivanovici and K. Mullen, *Angew. Chem., Int. Edit*., 49 (2010) 8408.
10. C. C. Li, Q. H. Li, L. B. Chen and T. H. Wang, *J. Mater. Chem.,* 21 (2011) 11867.
11. X. L. Yang, K. C. Fan, Y. H. Zhu, J. H. Shen, X. Jiang, P. Zhao and C. Z. Li, *J. Mater. Chem*., 22 (2012) 17278.
12. Y. P. Huang, Y. E. Miao, W. W. Tjiu and T. X. Liu, *RSC Adv*., 5 (2015) 18952.
13. B. Fu, X. Zhou and Y. P. Wang, *Mater. Lett*., 170 (2016) 21.
14. B. Li, X. M. Ge, F. W. T. Goh, T. S. A. Hor, D. S. Geng, G. J. Du, Z. L. Liu, J. Zhang, X. G. Liu and Y. Zong, *Nanoscale*, 7 (2015) 1830.
15. H. An, G. H. An and H. J. Ahn, *J. Alloys Compd*., 645 (2015) 317.
16. S. Abouali, M. A. Garakani, B. Zhang, Z. L. Xu, E. K. Heidari, J. Q. Huang, J. Q. Huang and J. K. Kim, *ACS Appl. Mater. Interfaces*, 7 (2015) 13503.
17. S. Abouali, M. A. Garakani, B. Zhang, H. Luo, Z. L. Xu, J. Q. Huang, J. Q. Huang and J. K. Kim, *J. Mater. Chem*. A, 2 (2014) 16939.
18. M. K. Yu, Y. X. Sun, H. R. Du, C. Wang, W. Li, R. H. Dong, H. X. Sun and B. Y. Geng, *Electrochim. Acta*, 317 (2019) 562.
19. M. H. Yang, J. M. Jeong, K. G. Lee, D. H. Kim, S. J. Lee and B. G. Choi, *Biosens. Bioelectron*., 89 (2017) 612.
20. Z. D. Wang, S. H. Qu, Y. H. Cheng, C. H. Zheng, S. Y. Chen and H. J. Wu, *Appl. Surf. Sci*., 416 (2017) 338.
21. X. Li, X. D. Tian, T. Yang, Y. Song, Y. M. Liu, Q. G. Guo and Z. J. Liu, *J. Alloys Compd.*, 735 (2018) 2446.
22. J. Liu, Z. Y. Li, X. G. Huo and J. L. Li, *J. Power Sources*, 422 (2019) 49.
23. B. Wang, X. Y. Lu, C. W. Tsang, Y. H. Wang, W. K. Au, H. F. Guo and Y. Y. Tang, *Chem. Eng. J*., 338 (2018) 278.
24. C. S. Yan, G. Chen, X. Zhou, J. X. Sun and C. D. Lv, *Adv. Funct. Mater*., 26 (2016) 1428.
25. S. J. Sun, X. Y. Zhao, M. Yang, L. L. Wu, Z. Y. Wen and X. D. Shen, *Sci. Rep*., 6 (2016) 19564.
26. Y. Shan and L. Gao, *Chem. Lett*., 33 (2004) 1560.
27. G. X. Wang, X. P. Shen, J. N. Yao, D. Wexler and J. H. Ahn, *Electrochem. Commun*., 11 (2009) 546
28. S. Q. Chen and Y. Wang, *J. Mater. Chem*., 20 (2010) 9735.
29. B. J. Li, H. Q. Cao, J. Shao, G. Q. Li, M. Z. Qu and G. Yin, *Inorg. Chem*., 50 (2011) 1628.
30. Y. T. Zhong, X. Wang, K. C. Jiang, J. Y. Zheng, Y. G. Guo, Y. Ma and J. N. Yao, *J. Mater. Chem*., 21 (2011) 17998.
31. J. X. Zhu, Y. K. Sharma, Z. Y. Zeng, X. J. Zhang, M. Srinivasan, S. Mhaisalkar, H. Zhang, H. H. Hng and Q. Y. Yan, *J. Phys. Chem*. C, 115 (2011) 8400.
32. J. Chen, X. H. Xia, J. P. Tu, Q. Q. Xiong, Y. X. Yu, X. L. Wang and C. D. Gu, *J. Mater. Chem*., 22 (2012) 15056.
33. Y. Gu, F. D. Wu and Y. Wang, *Adv. Funct. Mater*., 23 (2013) 893.
34. L. Shi, Y. Li, F. L. Zeng, S. J. Ran, C. Y. Dong, S. Y. Leu, S. T. Boles and K. H. Lam, *Chem. Eng. J*., 356 (2019) 107.
35. X. P. Liu, Z. H. Yang, Y. F. Zhang, C. C. Li, J. M. Dong, Y. Liu and H. S. Cheng, *Int. J. Hydrogen Energy,* 42 (2017) 10275.
36. J. Fang, Z. G. Xie, G. Wallace and X. G. Wang, *Appl. Surf. Sci.*, 412 (2017) 131.

37. D. W. Li, P. F. Lv, J. D. Zhu, Y. Lu, C. Chen, X. W. Zhang and Q. F. Wei, *Sensors,* 15 (2015) 29419.
38. B. C. Filiz and A. K. Figen, *Int. J. Hydrogen Energy*, 44 (2019) 9883.
39. J. Li, Y. Wang, S. Zhao, A. K. Jan, X. F. Zhang and X. Zhao, *J. Colloid Interface Sci*., 539 (2019) 442.
40. Z. Zeng, T. Zhang, Y. Y. Liu, W. D. Zhang, Z. Y. Yin, Z. W. Ji and J. J. Wei, *ChemSusChem*, 11 (2018) 580.
41. Y. J. Sun, Z. P. Wang, W. D. Wang, G. Li, P. W. Li, K. Lian, W. D. Zhang, S. Zhuiykov, J. Hu and L. Chen, *Mater. Res. Bull*., 109 (2019) 255.
42. M. S. Ata, R. Poon, A. M. Syed, J. Milne and I. Zhitomirsky, *Carbon*, 130 (2018) 584.
43. M. Yao, Z. P. Zeng, H. Zhang, J. H. Yan and X. B. Liu, *Electrochim. Acta*, 281 (2018) 312.
44. M. Taale, D. Kruger, E. Ossei-Wusu, F. Schutt, M. A. U. Rehman, Y. K. Mishra, J. Marx, N. Stock, B. Fiedler, A. R. Boccaccini, R. Willumeit-Romer, R. Adelung and C. Selhuber-Unkel, *ACS Biomater. Sci. Eng.*, 5 (2019) 4393.
45. M. Uceda, J. G. Zhou, J. Wang, R. Gauvin, K. Zaghib and G. P. Demopoulos, *Electrochim. Acta,* 299 (2019) 107.
46. R. L. Zhang, Y. Zhu, J. Huang, S. Xu, J. Luo and X. Y. Liu, *ACS Appl. Mater. Interfaces*, 10 (2018) 5926.
47. E. A. Jafari, M. Moradi, S. Hajati, M. A. Kiani and J. P. Espinos, *Electrochim. Acta*, 268 (2018) 392.
48. M. Farrokhi-Rad, *J. Alloys Compd*., 741 (2018) 211.
49. S. L. Allen and F. P. Zamborini, *Langmuir,* 35 (2019) 2137.
50. T. Battumur, S. B. Ambade, R. B. Ambade, P. Pokharel, D. S. Lee, S. H. Han, W. Lee and S. H. Lee, *Curr. Appl. Phys*., 13 (2013) 196.
51. S. H. Park and W. J. Lee, *Carbon,* 89 (2015) 197.
52. H. Fang, S. C. Zhang, X. M. Wu, W. B. Liu, B. H. Wen, Z. J. Du and T. Jing, *J. Power Sources*, 235 (2013) 95.
53. C. S. Du and N. Pan, *Nanotechnology*, 17 (2006) 5314.
54. Q. Wang, C. B. Wang, Z. Wang, J. Zhang and D. Y. He, *Appl. Phys. Lett*., 91 (2007) 141902.
55. F. C. Zheng and L. Z. Wei, *J. Alloys Compd*., 790 (2019) 955.
56. J. J. Deng, X. X. Lv, J. Zhong and X. H. Sun, *Appl. Surf. Sci.,* 475 (2019) 446.
57. M. K. Keshmarzi, A. A. Daryakenari, H. Omidvar, M. Javanbakht, Z. Ahmadi, J. J. Delaunay and R. Badrnezhad, *J. Alloys Compd*., 805 (2019) 924.
58. Y. T. Zhao, W. J. Dong, M. S. Riaz, H. X. Ge, X. Wang, Z. C. Liu and F. Q. Huang, *ACS Appl. Mater. Interfaces*, 10 (2018) 43641.
59. J. X. Shao, H. Zhou, M. Z. Zhu, J. H. Feng and A. H. Yuan, *J.* Alloys Compd., 768 (2018) 1049.
60. M. Zhong, W. W. He, W. Shuang, Y. Y. Liu, T. L. Hu and X. H. Bu, *Inorg. Chem*., 57 (2018) 4620.
61. Z. L. Chen, S. F. Wang, Z. B. Zhang, W. L. Zhou and D. J. Chen, *Electrochim. Acta*, 292 (2018) 575.
62. Z. F. Wang, X. Zhang, Y. Sun, C. P. Wang, H. Zhang, Y. H. Shen and A. J. Xie, *J. Alloys Compd.,* 740 (2018) 446.
63. X. L. Tong, M. Zeng, J. Li and Z. J. Liu, *J. Alloys Compd*., 723 (2017) 129.
64. D. Li, Q. F. Lu, E. Y. Guo, M. Z. Wei, Z. L. Xiu and X. Y. Ji, *J. Sol-Gel Sci. Technol*., 82 (2017) 75.
65. H. G. Wang, Y. J. Zhu, C. P. Yuan, Y. H. Li and Q. Duan, *Appl. Surf. Sci*., 414 (2017) 398.